29 July 2025

Cooperative Adaptive Junctions Govern Overall Photoelectrochemical Water Splitting

Aaron Kaufman[1,2,3], Kaden Wheeler[3,4], Ethan J. Crumlin[2], Shannon W. Boettcher[1,2,3]

1. University of California, Berkeley
2. Lawrence Berkeley National Laboratory
3. University of Oregon
4. University of California, Santa Barbara

Abstract

The solar-to-hydrogen conversion efficiencies for overall water splitting on particulate systems is low, below 3%. This limitation is in significant part due to the poor understanding, and thus inability to engineer, carrier-selective electron and hole contacts to the hydrogen- and oxygen-evolving electrocatalysts on the light-absorbing semiconductor particle. With dual-working-electrode and element-specific electric-potential measurements on $SrTiO_3$ model semiconductors by operando ambient-pressure X-ray photoelectron spectroscopy, we show that selective carrier collection emerges from cooperative adaptive junctions. Under illumination, hole collection by metal-oxide electrocatalysts drives metal cation oxidation that increases the effective interface electron barrier and improves hole selectivity. Simultaneously, electrons accumulate on metal hydrogen catalysts like Pt, forming hydridic species that lower the electron barrier. These findings challenge the idea that differences in crystal-facet work function govern charge separation and establish the new conceptual framework of cooperative adaptive junctions for improving particulate photocatalysts across materials systems.

Keywords

Cooperative adaptive junctions, Photoelectrochemical water splitting, SrTiO3 (STO), Operando ambient-pressure X-ray photoelectron spectroscopy (AP-XPS), Interfacial photovoltage

Cooperative Adaptive Junctions Govern Overall Photoelectrochemical Water Splitting

Aaron Kaufman[1,2,3], Kaden Wheeler[3,4], Ethan J. Crumlin[5,6*], Shannon W. Boettcher[1,2,3*]

[1] *Department of Chemical & Biomolecular Engineering and Department of Chemistry, University of California, Berkeley, CA 94720, USA*

[2] *Energy Storage and Distributed Resources Division, Lawrence Berkeley National Laboratory, Berkeley, CA 94720, USA*

[3] *Department of Chemistry and Biochemistry and the Oregon Center for Electrochemistry, University of Oregon, Eugene, OR 97403, USA*

[4] *Department of Chemistry and Biochemistry, University of California, Santa Barbara, CA 93106, USA*

[5] *Chemical Sciences Division, Lawrence Berkeley National Laboratory, Berkeley, CA 94720, USA*

[6] *Advanced Light Source, Lawrence Berkeley National Laboratory, Berkeley, CA 94720, USA*

Abstract:

The solar-to-hydrogen conversion efficiencies for overall water splitting on particulate systems is low, below 3%. This limitation is in significant part due to the poor understanding, and thus inability to engineer, carrier-selective electron and hole contacts to the hydrogen- and oxygen-evolving electrocatalysts on the light-absorbing semiconductor particle. With dual-working-electrode and element-specific electric-potential measurements on $SrTiO_3$ model semiconductors by *operando* ambient-pressure X-ray photoelectron spectroscopy, we show that selective carrier collection emerges from cooperative adaptive junctions. Under illumination, hole collection by metal-oxide electrocatalysts drives metal cation oxidation that increases the effective interface electron barrier and improves hole selectivity. Simultaneously, electrons accumulate on metal hydrogen catalysts like Pt, forming hydridic species that lower the electron barrier. These findings challenge the idea that differences in crystal-facet work function govern charge separation and establish the new conceptual framework of cooperative adaptive junctions for improving particulate photocatalysts across materials systems.

Main

Overall water splitting (OWS) on photocatalyst particles converts solar to chemical energy without wires[1-3]. Both the optoelectronic properties (including light absorption, carrier lifetimes and mobilities, etc.) of the semiconductor photocatalyst, and the carrier-selective contacts used to extract the photoexcited holes that drive oxidation and electrons that drive reduction reactions, are key parameters that govern performance[4]. $SrTiO_3$ (STO) is a widely studied OWS photocatalyst that can yield external quantum efficiencies of up to 96% with ultraviolet (UV) light. However, STO exhibits poor solar-to-hydrogen conversion efficiencies with visible light because it has a large bandgap of 3.2 eV. Bandgap engineering via cation or anion substitution improves solar absorption, but not solar-to-hydrogen conversion efficiency[2,5-7]. Oxides with narrower bandgaps, including $BiVO_4$, Fe_2O_3, and TaON,[8-11] have better solar absorption, but do not generate sufficient photovoltage for OWS, even with band gaps > 2 eV[8-11]. If these absorbers were coupled to optimally selective electrocatalyst contacts, they likely could drive OWS with much higher efficiency than STO[12]. Unfortunately, the processes that govern charge separation and selective carrier collection at particulate semiconductor surfaces are poorly understood.

The influence of crystal-facet termination on photocatalytic activity has received much attention,[13-15] with electron-hole separation attributed to differences in work function between facet orientations. Multiple studies report increased OWS rates when specific facets are exposed where hydrogen-evolution-reaction (HER) catalyst particles decorate lower-work-function facets and collect electrons while oxygen-evolution (OER) catalysts decorate higher-work-function facets and collect holes[1,3,9,14]. Consistent with facet-dependent carrier collection, nanoprobe measurements showed asymmetric *J-V* curves when measured across different exposed facets (<100>, <110>, and <111> on nanoparticles, see **Figure S1**) with single-crystal studies on STO yielding similar asymmetries[13,16,17]. These results indicate asymmetric charge transport due to different barriers for electrons and holes associated with the different work functions between facets. This physical picture has been used to explain the near-unity quantum efficiency of OWS on STO with HER/OER catalysts selectively decorated on each appropriate facet[3].

While the observed differences in work function likely drive a degree of asymmetric carrier collection, the magnitude of the difference is insufficient for explaining OWS. The voltage across opposing crystal facets (acting as selective contacts) must significantly exceed 1.23 V for OWS to proceed under standard conditions, but the difference in facet work functions, and thus barrier heights, is no more than 200 mV[13,18]. Based on the established physics of photovoltaic action, the difference in barriers is the physical limit for the photovoltage developed across the hole and electron contacts[19-21]. However, we have demonstrated that at both hole- and electron-selective semiconductor/electrocatalyst junctions on *n*- and *p*-type semiconductors, respectively, the rates of interfacial charge transfer are not solely dictated by equilibrium junction properties[22-27]. Electrocatalysts are complex materials that undergo ion insertion, redox, and surface absorption when driven to catalytic conditions that modify both the effective work function and the underlying contact properties to the semiconductor light absorber.

Here we show that cooperative adaptive electrocatalyst–semiconductor (cat|sem) junctions, rather than crystal facet asymmetry, are the key drivers of charge separation in *operating* STO-based photocatalysts. We use single-crystal substrates doped with oxygen vacancies to increase conductivity (*n*-STO) as a model system and apply both dual-working-electrode and *operando* ambient-pressure X-ray photoelectron spectroscopy (AP-XPS)[28,29] measurements to track dynamic junction properties and interfacial photovoltages. We find that Pt and CoO_x contacts simultaneously and dynamically modulate their interfacial energetics under operation. This simultaneous and mutually dependent process appears required, in addition to crystal-facet asymmetry, to generate the photovoltage required for OWS on STO and related systems.

Crystal facet asymmetry in selective carrier collection for OWS. Facet-specific carrier selectivity may drive initial charge separation to begin electrochemical charging of the two catalysts. The differences in work function on the dominant <100> and <110> facets of bare (without added electrocatalyst) *n*-STO are established[3,13-16,18]. Larger flat-band potentials are observed at <110>-oriented *n*-STO than at <100>-oriented *n*-STO, having a difference of 0.16 V with a ferri/ferrocyanide redox couple[13]. Illuminated cyclic voltammetry indicates larger photovoltages for <110> *n*-STO photoanodes driving the OER[13]. We found similar differences in crystal-facet work function and resulting photovoltages on bare *n*-STO in 1.0 M NaOH (**Figure 1**). The commercially epi-polished single crystals of STO, reduced together in H_2, used here yielded similar *n*-type oxygen-vacancy doping concentrations (evident from the Mott–Schottky slopes in the **Figure 1** inset, $N_d = 1.7 \times 10^{19}$ cm^{-3} for <110> and 1.4×10^{19} cm^{-3} for <100>). The <110>-oriented *n*-STO shows ~150 mV more-negative flat-band potential than the <100>-oriented *n*-STO and thus a ~150 mV larger photovoltage than the reversible potential for OER at 1.23 V vs. RHE which persists as a function of pH (**Figure S2**). To test if the facet asymmetry alone can drive OWS, we shorted the two ohmic contacts of the <110>- and <100>-oriented photoelectrodes together, and as expected, detected no OWS photocurrent (**Figure S3**) due to inadequate barrier-height asymmetry. Photocurrent was observed only before N_2 sparging, likely due to O_2 reduction at the cathode (<100>) and OH^- oxidation at the anode (<110>), indicating a regenerative electrochemical process rather than a photosynthetic one[30].

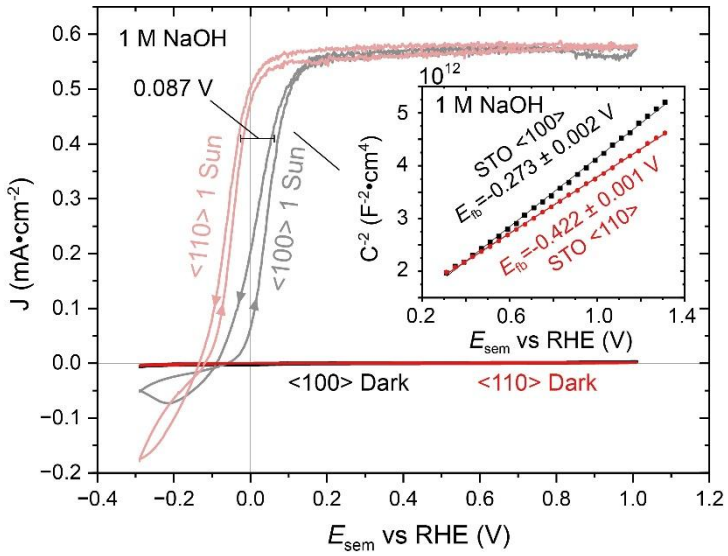

Figure 1. Comparison of hole collection at different crystal facets. Dark and light (approximately one sun of solar simulation) cyclic voltammetry curves of bare *n*-STO in 1.0 M NaOH. The inset shows Mott–Schottky analyses in the same electrolyte under dark conditions. Both results indicate that the small crystal-facet asymmetry is not sufficient to drive OWS.

Although the crystal-facet carrier-collection asymmetry is not sufficient for driving OWS, it does appear to be important.[13,14,31] For particulate STO, catalyst loading on specific facets, such as Pt on the <100> facet and CoO_x on the <110> facet, improves quantum efficiency[1,3,14,31]. Prior to the OWS studies, electrocatalysts are typically selectively deposited onto specific crystal facets by photodeposition, often called photolabeling[14,31]. This process is an indication that the asymmetries are sufficient to drive initial charge separation and generate a small photovoltage. We found individual Pt nanoparticles deposited on different crystal orientations of *n*-STO had Schottky barrier heights with an average difference less than ~100 mV using conductive atomic force microscopy (**Figure S4**). This suggests that even at the nanoparticle scale, with the influence of local environments (i.e. pinch-off effect, surface defects, etc.), the work-function difference between crystal facets is small when (photo)electrochemical reactions are not being driven. Therefore, while crystal-facet asymmetry alone cannot explain OWS on STO, experimental evidence does indicate the asymmetry is sufficient to drive initial selective materials deposition reactions, such as Pt plating, which requires little photovoltage.

Simulations of cooperative adaptive junctions. We hypothesized that the facet-asymmetry drives selective deposition of different catalyst material and that under photoexcitation, the local cathode and anode catalysts each change their junction properties with the semiconductor as they start to accumulate electrons and holes. If the chemical potentials and barrier heights both dynamically adjust to match the redox potentials of the reactions being driven, this could lead to large photovoltages at steady state. We term these cooperative adaptive cat|sem junctions.

We used numerical simulations to assess the possible role of cooperative adaptive junctions in OWS, where two catalysts are attached to a single semiconductor

photoabsorber such as STO. **Figure S5** compares simulated current-voltage curves for adaptive junctions ($J_{\mathrm{jxn,adapt}}$) to those of the traditional buried junction ($J_{\mathrm{jxn,buried}}$). Equations 1.1 and 1.2 were used to model the interfacial currents following our previously studies[25] that make use of simple Butler–Volmer kinetic models. The fraction of the voltage dropped in the electrolyte vs. in the semiconductor was calculated using Equation 1.3[25].

$$J_{\mathrm{jxn,buried}} = k_{\mathrm{p}}\left(p'_{\mathrm{s}} - p_{\mathrm{s}}\right) - k_{\mathrm{n}}\left(n'_{\mathrm{s}} - n_{\mathrm{s}}\right) \tag{1.1}$$

$$J_{\mathrm{jxn,adapt}} = k_{\mathrm{p}}\left(p'_{\mathrm{s}} - p_{\mathrm{s}}e^{\frac{qV_{\mathrm{cat}}}{kT}}\right) - k_{\mathrm{n}}\left(n'_{\mathrm{s}} - n_{\mathrm{s}}e^{\frac{-qV_{\mathrm{cat}}}{kT}}\right) \tag{1.2}$$

$$J_{\mathrm{cat}} = j_{0,\mathrm{cat}}\left(e^{\frac{qV_{\mathrm{cat}}}{2kT}} - e^{\frac{-qV_{\mathrm{cat}}}{2kT}}\right) \tag{1.3}$$

The terms q, K, and T are the fundamental charge, Boltzmann's constant, and absolute temperature , respectively; k_{p} and k_{n} are the rate constants for interfacial hole and electron transfer, respectively; p'_{s} (n'_{s}) and p_{s} (n_{s}) are the steady-state and equilibrium surface hole (electron) concentrations, respectively. For the adaptive junction, the (pseudo)equilibrium electron and hole concentrations are modified by the state of the catalyst (V_{cat}), which changes under operation. The value of p_{s} is found from the generalized Gärtner equation that accounts for transport and recombination in the illuminated semiconductor[32]. The full simulation code is given in the Supplementary information.

We simulate two different contacts to *n*-type STO. The Pt contact must, under steady-state conditions, selectively collect electrons and drive HER. CoO_x must selectively collect holes and drive OER. The simulations shown in **Figure S5** predict that if electrons accumulate on Pt particles and the Pt | *n*-STO junction is of the adaptive type, it will become more ohmic (electron selective) as the Pt Fermi level rises on the vacuum scale. This is distinct from the static buried-junction case in which charge separation and catalysis are series processes modelled by an equivalent circuit with a constant photodiode element. Below, we discuss experimental data mechanisms through which the Pt | *n*-STO junction may yield such a response.

Experiments also suggest adaptive junction behavior is expected for electrodeposited CoO_x on STO because transition-metal redox chemistry is coupled with ion movement inside the electrocatalyst to balance charge[23,25,33,34]. Simulating the CoO_x | *n*-STO junction with the adaptive-junction model, we predict a dynamic change in the barrier height as CoO_x is oxidized (that is, E_{cat} moving lower in **Figure 2**), becomes more selective for holes, and thus generates a larger photovoltage. In **Figure 2** the degree of band bending and the distance to the vacuum level (E_{vac}) reflects the electrostatic potential distribution throughout the junction (**Figure S5**). The simulations show that within the adaptive junction limit, photovoltages at the OER catalyst junction with *n*-STO are larger than for typical (unoptimized) buried junctions.

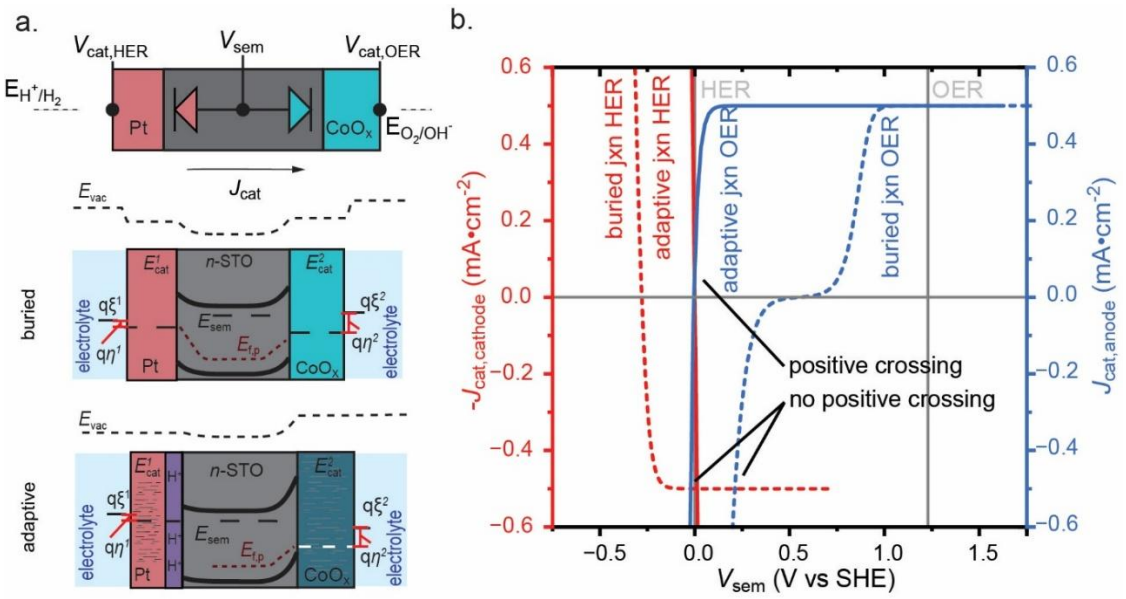

Figure 2. Dual adaptive junctions. Pt | *n*-STO | CoO_x (**a**) buried (dashed) and adaptive-junction (solid) schematic and band-bending diagrams depicting the formal potential of electrochemically active species in the electrolyte ($q\xi$, with superscripts indicating each electrolyte, 1 or 2), the kinetic overpotential (η), and the hole Fermi level with ($E_{f,p}$) and without (E_{sem}) illumination. (**b**) Numerical simulation of buried and adaptive junctions taking as examples $J_{0,cat}$ = 1 and 10^{-3} mA · cm^{-2} for Pt and CoO_x driving the HER (red) and OER (blue), respectively. J_{HER} and J_{OER} must be equal and opposite at steady state for this system to drive OWS[11]. Simulated buried junctions and combinations of buried and adaptive junctions were not observed to develop sufficient photovoltage to drive OWS. Only the cooperative (dual) adaptive junctions in this simulation, with modest effective barrier heights of 0.4 and 1.9 eV, were observed to drive OWS, as shown in (**b**) inset.

A OWS photocatalyst must drive two half reactions, here the HER and the OER. To simulate OWS, we required the OER and HER cat|sem junction currents to be equal and opposite at steady state (**Figure 2**), similar to the conditions outlined in Takata et. al[3] for near-unity quantum efficiency. For the reaction $2H_2O \rightarrow 2H_2 + O_2$ to proceed, the magnitudes of the oxidation and reduction current densities must be equal for a given V_{sem} (**Figure 2b**). The non-adaptive-junction systems have small V_{oc} constrained by the static work function difference of the contacts, resulting in lower efficiency and no single V_{sem} that meets the criteria for driving both half reactions simultaneously. In contrast, the adaptive photoanode junctions provide increased V_{oc}, while the photocathode junction becomes ohmic, both because the electrocatalyst work function becomes a function of the current driving through the contact.

The OWS current, represented by the crossing of the two *J-E* relationships, is defined by the OER and the HER cat|sem junction independently for a given common V_{sem}. We did not observe a positive crossing of the reduction and oxidation current densities, even when one adaptive with one buried junction were used. These simulations suggest that both the HER and the OER electrocatalysts, Pt and CoO_x, respectively, must form adaptive junctions to drive OWS on STO.

Experimental assessment of adaptive junctions on single-crystal STO. To test if CoO_x and/or Pt form adaptive junctions on *n*-STO, the dual-working-electrode technique[26,27] was

used to study each cat|sem interface during operation. Here the catalyst, either CoO_x or Pt, was held at a potential E_{cat} vs. the reference electrode, setting its chemical/redox state. We used commercial epi-polished STO reduced under H_2 at 1000 °C for 6 h to form O vacancies and increase *n*-doping and conductivity. A direct electrical contact to the catalyst layer was then used to set E_{sem} vs. E_{cat} using a second potentiostat channel, and the resulting current through the semiconductor J_{sem} was measured. The resulting J-V_{app} curves were fit to the Schottky diode equation, and the barrier height ϕ_b extracted was plotted vs. E_{cat} (**Figure 3**).

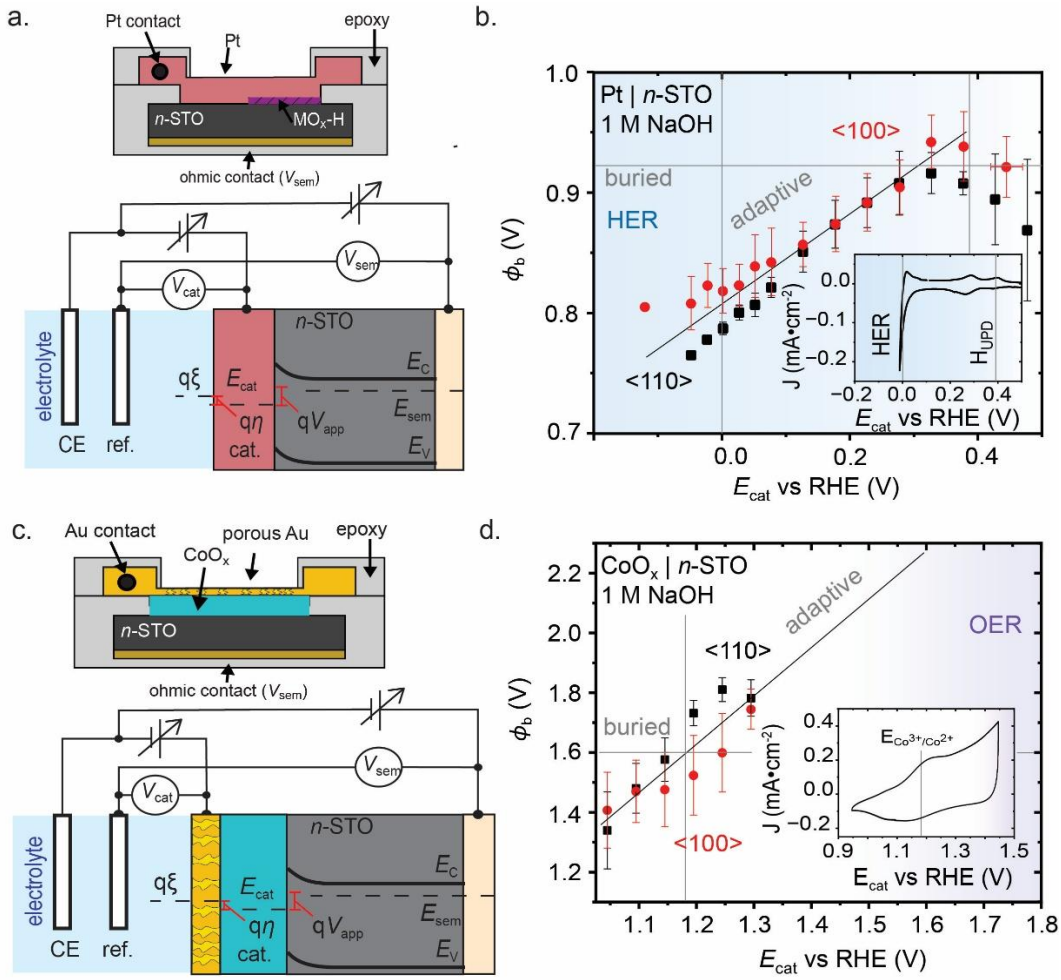

Figure 3. Electrical measurements of adaptive junctions. Panels (**a**) and (**c**) display the device geometry used for the DWE measurements on Pt | *n*-STO and CoO_x | *n*-STO junctions, respectively, for both <100> (red circles) and <110> (black squares) oriented single crystals. Panel **(a)** highlights the growth of a proton-rich interface (MO_x-H) in purple when the electrocatalyst is driving the HER. Panel (**b**) shows the electron barrier height from the Pt | *n*-STO junctions, and **(d)** shows the electron barrier height from the CoO_x | *n*-STO junctions, both of which were calculated from the *J*-*V* curves where the total current through the junction was measured vs the potential across the junction (V_{app}) as a function of catalyst potential (E_{cat}) in 1.0 M NaOH. Values of E_{cat} > 1.3 V in the CoO_x | *n*-STO experiments caused the thin film to break up. In both (**b**) and (**d**), the data points are the average of three separate experiments and the error bars indicate the standard deviation. Mott-Schottky plots for the interfaces using the DWE setup are in **Figure S7**.

As the Pt catalyst is held at a more-negative E_{cat}, particularly as it approaches the RHE and Pt starts to form Pt-H and evolve H_2, the apparent Φ_b at Pt | *n*-STO decreases with a slope of $d\Phi_b/dE_{cat}$ = 0.35 ± 0.02 V (**Figure 3b**). As the CoO_x catalyst is held at more-positive E_{cat}, approaching and into the OER region, the apparent Φ_b at CoO_x | *n*-STO increases with a slope of $d\Phi_b/dE_{cat}$ = 1.4 ± 0.3 V (**Figure 3d**).

These DWE results show that both the metal-HER and oxide-OER catalysts create adaptive junctions with STO on both the dominant crystal facets. The behavior of CoO_x is analogous to that of other oxide/(oxy)hydroxide catalysts previously studied on oxide semiconductors[25,26]. CoO_x catalysts typically convert from $Co(OH)_2$ to CoOOH with increasing nominally Co^{4+} density as the potential is driven positive for the OER[33,34]. As the redox-state changes, the CoO_x exchanges ions with the electrolyte to compensate the electronic charge, similar to a battery electrode material, forming adaptive junctions that increase in barrier height as holes accumulate (increasing hole selectivity; **Figure 3c**) [25].

The adaptive behavior of Pt | *n*-STO is more surprising. Pt is a solid ion-blocking metal that does not undergo bulk redox chemistry as it drives the HER but forms surface Pt-H [35-37]. The Pt | *n*-STO interface is likely hydrated with water and mobile ions in the electrolyte, as the Pt was deposited at room temperature by electrodeposition. The adaptive junction behavior of Pt is likely due to both ion accumulation and Pt-H formation at the Pt | *n*-STO interface, which screens electronic charge placed on Pt, lowering its apparent steady-state barrier height compared to that at equilibrium. A similar effect was observed at the Pt | *n*-STO interface in H_2 gas (**Figure S6**). As this process changes the band bending in the semiconductor, and thus the density of majority carriers at the interface, it is also the basis for classes of solid-state H_2 gas sensors[38]. The observation that Pt | *n*-STO has $d\Phi_b/dE_{cat}$ = 0.35 ± 0.02 V, far less than unity, indicates that the screening of the electronic charge in Pt by ions or surface absorbates is only partially effective. The electronic charge in CoO_x, which can (de)insert ions into the bulk structure[39-41], appears fully screened with $d\Phi_b/dE_{cat}$ = 1.4 ± 0.3 V (the limit is $d\Phi_b/dE_{cat}$ = 1 within the physical model used to explain the behavior; there may be other non-idealities and uncertainties in the quantitative value).

AP-XPS measurement of cooperative adaptive junctions. The above studies on the individual Pt | *n*-STO and CoO_x | *n*-STO junctions show notable adaptive-junction behavior. Based on the simulations discussed above, these adaptive cat|sem junctions could explain how small facet-dependent differences in carrier selectivity are amplified to provide the photovoltage necessary for OWS.

We next assessed whether cooperatively adaptive-junction behavior can be observed on single-crystal STO model systems without wires or external bias. Tracking material-specific electric potentials across surfaces is difficult with conventional electrochemical techniques, particularly when complementary half reactions occur on the same surface, such as in STO <111>undergoing OWS and collecting both electrons and holes at spatially distinct sites on the surface.[42] AP-XPS analysis provides information on both the chemical and electrostatic environment in an element-specific manner and can be performed through a thin electrolyte layer[28,29,43,44].

Here, we used commercial epi-polished STO reduced in H_2 atmosphere as in the DWE experiment. We introduced HER and OER sites by photodeposition of Pt and CoO_x, respectively, creating a planar, single-crystal analog to the OWS particles (**Figure S8**)[3,14]. Like Rh | *n*-STO | CoO_x, the Pt | *n*-STO | CoO_x particles can drive OWS in pure water and aqueous electrolyte[3,14,31]. Early work by Wagner and Somorjai also showed OWS on single-crystal STO <111> that was sensitive to surface composition and OH^- concentration[42,45].

The initial work-function difference between Pt and CoO_x is expected to be less than 1.23 V. Pt has a high work function of 5.6 – 5.8 eV. The work function of CoO_x is similarly large and varies from 5.2 - 6.2 eV depending on composition and oxidation state. Given the physical picture presented above, these contacts would not be able to support carrier collection for OWS without the formation of adaptive junctions where their work functions change during operation.

AP-XPS measurements revealed that the environmental conditions control the cat|sem junction properties. Under high vacuum, no significant light-induced changes were observed in the Pt 4f and Co 2p 3/2 spectra (**Figure 4a**). The Pt features (including those corresponding to the metal and oxide states) were observed to be *electrostatically* shifted to higher binding energies than their expected positions, indicating selective hole collection from X-ray generated carriers. The collection of holes from STO by Pt is consistent with the large Pt workfunction,[36,46] but is inconsistent with the Pt serving as a HER site collecting electrons during OWS. CoO_x showed strong Co^{2+} character, with the presence of a Co^{2+} satellite feature, indicating a lack of hole collection.

The catalyzed STO was then exposed to 18 torr water vapor (saturated at room temperature). Again, no large changes were observed in the Pt 4f and Co 2p spectra between light and dark cycling (**Figure 4b**). The Co^{2+} satellite feature decreased in intensity compared to high-vacuum, likely due to increased coordination of CoO_x with surface water. The Pt spectra contained proportionally more metallic Pt^0. The Pt-related binding energies remained positively shifted, again indicating hole collection on Pt. This result is consistent with Wagner's study[42], in which water splitting was not observed in water vapor alone.

With the addition of surface KOH and 18 torr water vapor, notable transitions are observed in the AP-XPS spectra (**Figure 4c**). Under solar simulation, the Pt 4f spectra lose their highest oxidation peak, and the Pt^0 peak shifted to lower binding energies. This negative shift indicates that Pt now functions as an electron collector. The Pt^0 4f peak under simulated solar illumination aligns with both the accepted literature value and the internal metal reference. This result is consistent with the data in **Figure 3** that outlines a reduction in the electron barrier, making the contact more ohmic. The shifts were reproducible under dark/light cycling. Although Pt-H formation occurs on the electrode surface during the HER, and has been observed in small amounts via *operando* AP-XPS in KOH[36], the shift to lower binding energies shown in **Figure 4** are unlikely due to Pt-H formation but associated with the Pt | *n*-STO interface becoming ohmic. This is because the amount of formed Pt-H is small and the complete transformation required to shift the peak via chemical change has not been observed in controlled studies of Pt driving HER in KOH[36]. In contrast, the Co 2p spectrum shows an obvious transition to an oxidized state with KOH present, shifting from

Co^{2+} to Co^{3+}, as confirmed by the attenuation of the Co^{2+} satellite feature at 785–787 eV. Thus, CoO_x now serves as a hole collector[47].

The combination of KOH and water vapor, providing a path for ion-transport through a surface-electrolyte phase and electron transport through the solid, enables the concomitant oxidation of CoO_x and reduction of Pt upon illumination. Pt, which formed a large-barrier Schottky contact with *n*-STO, collected *holes* in vacuum/water but switched to collecting electrons once ions were present to allow for the coupled photooxidation of $Co(OH)_2$ to CoOOH.

Central to this interpretation is the finding that Pt^0 shifted to lower binding energies in the Pt 4f spectra (collecting electrons) only when coupled with oxidation of $Co(OH)_2$ to CoOOH. This likely proceeded at reconstructed surface-defect sites, commonly observed at all dominant single-crystal terminations of STO[48-51]. We thus hypothesize that local (within the minority-hole-diffusion length) electron- and hole-selective adaptive contacts enable the collection and conversion of the electrocatalyst to the active phase for their intended redox reactions in a positive feedback loop.

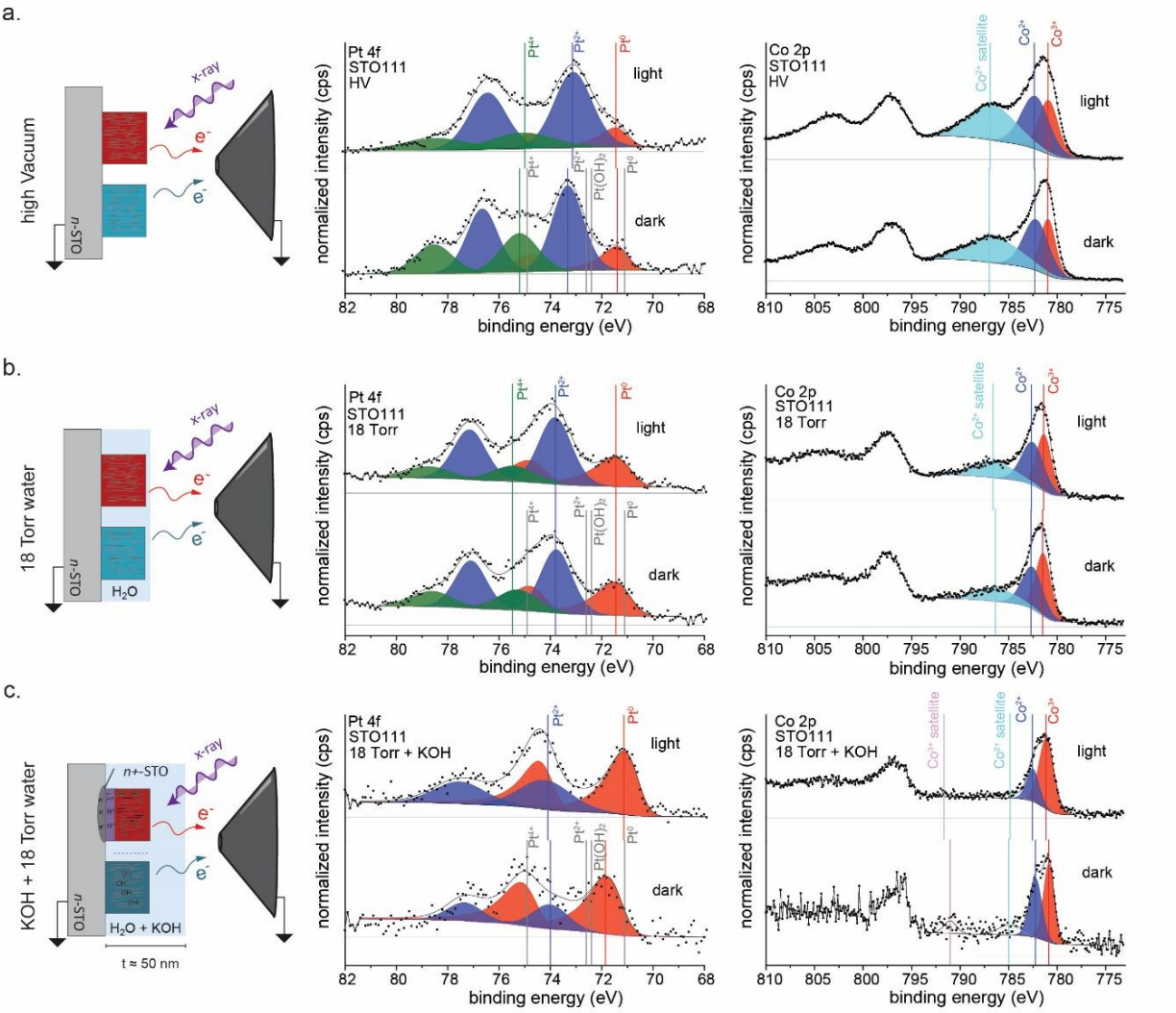

Figure 4. Adaptive junction and photovoltage measurements by AP-XPS. The left-most diagrams on panels **(a)**, **(b)**, and **(c)** respectively illustrate high-vacuum AP-XPS conditions, 18 Torr water vapor, and 20 µL 0.0133 M KOH in 18 Torr water vapor. The data was collected at 4 keV photon energy under grazing incidence (<1°) with dark then light cycling. All gray vertical lines in the spectra labeled "dark" indicate literature values for present oxidation states. Colored lines in the top "light" spectra indicate the fitted species (Co 2p spectra in 18 Torr + KOH was loosely fitted with Co^{2+} or Co^{3+} satellite peaks to indicate their expected locations, but this is intended only for qualitative demonstration of their position). An internal gold foil was used as an energy reference for all respective atmospheric conditions. The analyzer was shorted to the Au reference and the ohmic back contact of the *n*-STO samples established with Ga-In eutectic enclosed in vacuum-compatible epoxy. Analogous data for <100> and <110> STO is in **Figures S9** and **S10,** and <111> STO O 1s data is in **Figure S11.**

The role of cooperative adaptive junctions in OWS. Collectively, the data here indicates a new coupled mechanism of carrier separation and collection in particulate photocatalysts (**Figures 5 and S12**). Crystal-facet asymmetry is unlikely to play a central role in separating charge carriers under co-catalyzed OWS conditions. Instead, the crystal-facet asymmetry may provide the initial conditions that set up positive feedback loop that improves charge separation to the two catalyst sites. First, both electrocatalysts are photodeposited onto the

crystals without external electrical biasing. Upon illumination, Pt is reduced preferentially on sites where there is a higher concentration of photogenerated electrons, and CoO_x precursors are oxidatively deposited at locations of larger hole concentrations. Once the catalysts are deposited, they further increase their selectivity for their respective carrier as they accumulate the reductive or oxidative charge needed to drive the HER or the OER, respectively. This process would continue to increase selectivity until a steady state is reached. These changes in chemistry, work function, and barrier height may thus yield a self-reinforcing charge-separation mechanism much different than the buried Schottky-junction model[52,53].

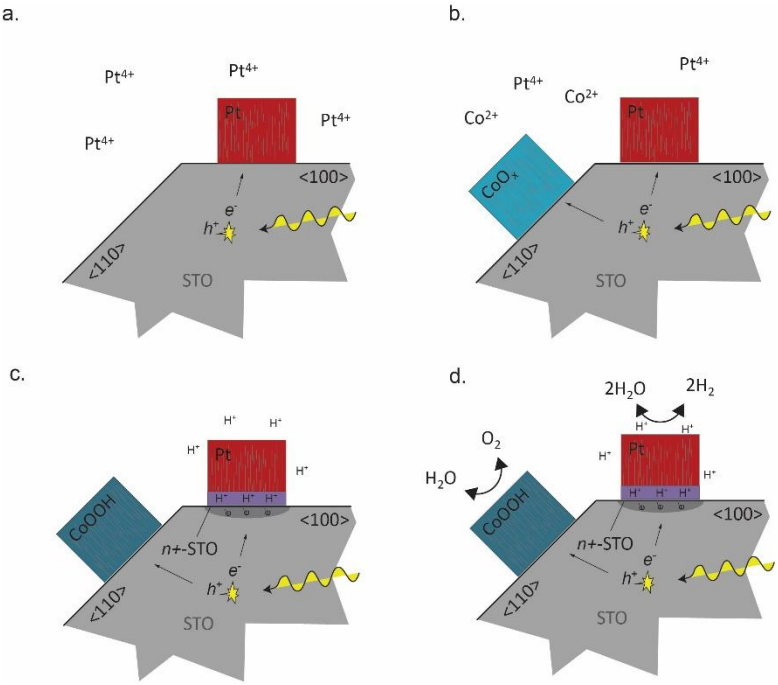

Figure 5. Mechanism of cooperative adaptive junction formation in STO-based overall water splitting (OWS) particles. (a) Faceted $SrTiO_3$ (STO) particles are immersed in a solution containing first a Pt^{4+} precursor, illuminated and Pt is selectively deposited on the <100> facet. **(b)** Under illumination and now with both precursors in the solution, crystal facet asymmetry drives initial charge separation, enabling selective photodeposition with CoO_x oxidatively deposited on <110> facets. **(c)** Upon continued illumination, the deposited catalysts begin to form adaptive junctions. Pt accumulates surface protons and Pt-H species, and CoO_x transitions to CoOOH through oxidative ion insertion and valence change. (**d)** At steady state, both electrocatalysts cooperatively maintain asymmetric junction energetics, Pt functions as an electron-selective HER site, and CoOOH as a hole-selective OER site, enabling light-driven overall water splitting.

These results establish new engineering principles for OWS systems. (1) Carrier-selective junctions must be designed with consideration of adaptive-catalyst mechanisms that allow for electrolyte/ion permeation either through, as in CoO_x, or around, as in Pt/Pt-H structures. Photochemical deposition methods of both metal or metal oxide electrocatalysts onto semiconductor absorbers likely provide better adaptive junction interfaces due to the lack of a buried heterojunction that cannot be accessed by ions or chemical species. Alloys of Pt, for example with Pd that form bulk hydrides, might allow for

improved adaptive junctions due to better charge screening. (2) Ion transport across the semiconductor-electrocatalyst interface must be explicitly considered, as ion motion directly impacts charge separation and formation of the effective selective contacts. (3) Facet-selective catalyst deposition can be leveraged to trigger positive feedback loops in interfacial carrier selectivity, increasing photovoltage. (4) Interface properties measured ex-situ are insufficient to understand carrier collection under OWS.

These principles are applicable to lower-bandgap particulate photocatalysts that can achieve high solar conversion efficiency once their interfacial selective hole and electron contacts are improved.

Methods:

Single-crystal STO fabrication: $SrTiO_3$ intrinsic single crystals were purchased from Crystal Substrates and MTI epi-polished (single side) with an offcut of <0.5°. Samples were then reduced in a H_2 furnace at 1000 °C for 6 h. Ohmic contacts were produced by rubbing Ga-In eutectic on the unpolished face; subsequently, a wire with Ag paste was used to make an electrical connection. Electrodes were sealed in chemically resistant and vacuum-compatible epoxy (Hysol Loctite 9460).

Simulation: The governing equations were solved numerically by SciPy's fsolve and root_scalar functions. These functions use Newton's method with a scaled gradient approach and Brent's method with a hybrid root finding algorithm to iteratively solve systems of nonlinear equations, requiring an initial guess and assuming local differentiability.

DWE electrode fabrication: DWE configurations used reduced STO with an ohmic back contact using Ga-In eutectic and were encased in epoxy to expose only the polished single-crystal surface.

(Pt DWE): With the sides of the epoxy masked, 40 nm Pt was deposited by electron-beam evaporation at 0.2 Å/s. A tinned-copper wire was then connected to the Pt thin film on the epoxy with a small amount of Ag paste, and the wire and electrode were encased again in epoxy, with only the active area of the sample exposed.

(Co DWE): With the sides of the epoxy masked, 2 nm of Co was deposited by electron-beam evaporation 0.2 Å/s. Excess CoO_x was photodeposited onto the electrode surface from a 1 M $CoCl_2$ solution buffered to pH 9.5 with K-borate solution by applying +1 V vs. SCE for 90 s. The electrode was then cycled for 25 cycles at 50 mV/s in the dark then 25 cycles under 1 sun to fully convert the CoO_x film to redox-active $Co(OH)_2$/CoOOH. The solar simulator (HAL-320 Solar Simulator, Asahi Spectra USA Inc.) output was measured with a UV005 photodiode. A 10 nm porous Au film was then deposited by thermal evaporation to create an electrolyte-permeable top contact and to enable electrochemical control the oxidation state of the catalyst film. A tinned-copper wire was then connected to the Au thin film on the epoxy with a small amount of Ag paste. Subsequently, the wire and electrode were encased again in epoxy, with only the active area of the sample exposed.

AP-XPS: The Advanced Light Source beamline 9.3.1 was used for all AP-XPS experiments. A photon energy of 4 keV was used for all pressures and sample conditions. Pt and CoO_x electrocatalysts were sequentially deposited from H_2PtCl_6 and $CoCl_2$, respectively, on reduced STO (*n*-STO). To observe light-induced effects, all viewports were covered except for the solar simulator's quartz viewport. An extreme grazing incidence (<1°) was used to decrease the X-ray flux. The solar simulator (HAL-320 Solar Simulator, Asahi Spectra USA Inc.) light output measured with a UV005 photodiode in-situ at the sample was approximately 0.1 sun or 10 mW/cm^2). Between each atmospheric condition, a new sample location was chosen, and each comparative spectra had a similar amount of beam exposure. An internal gold foil was used as an energy reference for all respective atmospheric conditions. The analyzer was shorted to the Au reference and the ohmic back contact of the STO samples established with GaIn eutectic enclosed in vacuum-compatible epoxy.

Data availability

All data that support the findings of this study are included in the article and its Supplementary Information.

Acknowledgements

The work was primarily supported by Department of Energy, Basic Energy Sciences grant no. DE-SC0014279. The AP-XPS analysis portion of the work was also supported by a DOE SCGR fellowship, DOE SCGSR 2023 S1. The AP-XPS analysis portion of the work was also supported by the Liquid Sunlight Alliance which is funded by the U.S. Department of Energy, Office of Science, Office of Basic Energy Sciences, Fuels from Sunlight Hub under Award Number DE-SC0021266.

Author information

A.K. performed the experiments with assistance from K.W. E.J.C. helped with characterization and AP-XPS analysis. S.W.B. initiated and supervised the work. A.K. wrote the paper. All authors participated in scientific discussions and manuscript and figure prepartion and revision.

Correspondence to Shannon W. Boettcher (boettcher@berkeley.edu) and Ethan J. Crumlin (ejcrumlin@lbl.gov).

Ethics declarations

Competing interests: The authors declare no competing interests.

References:

1 Chen, S., Takata, T. & Domen, K. Particulate photocatalysts for overall water splitting. *Nature Reviews Materials* **2**, 17050 (2017).

2 Takata, T. & Domen, K. Particulate Photocatalysts for Water Splitting: Recent Advances and Future Prospects. *ACS Energy Letters* **4**, 542-549 (2019).

3 Takata, T., Jiang, J., Sakata, Y., Nakabayashi, M., Shibata, N., Nandal, V., Seki, K., Hisatomi, T. & Domen, K. Photocatalytic water splitting with a quantum efficiency of almost unity. *Nature* **581**, 411-414 (2020).

4 Kaufman, A. J., Nielander, A. C., Meyer, G. J., Maldonado, S., Ardo, S. & Boettcher, S. W. Absolute band-edge energies are over-emphasized in the design of photoelectrochemical materials. *Nat. Catal.* **7**, 615-623 (2024).

5 Jiang, J., Kato, K., Fujimori, H., Yamakata, A. & Sakata, Y. Investigation on the highly active SrTiO3 photocatalyst toward overall H2O splitting by doping Na ion. *Journal of Catalysis* **390**, 81-89 (2020).

6 Iwase, A., Yoshino, S., Takayama, T., Ng, Y. H., Amal, R. & Kudo, A. Water Splitting and CO2 Reduction under Visible Light Irradiation Using Z-Scheme Systems Consisting of Metal Sulfides, CoOx-Loaded BiVO4, and a Reduced Graphene Oxide Electron Mediator. *J Am Chem Soc* **138**, 10260-10264 (2016).

7 Kato, H., Sasaki, Y., Shirakura, N. & Kudo, A. Synthesis of highly active rhodium-doped $SrTiO_3$ powders in Z-scheme systems for visible-light-driven photocatalytic overall water splitting. *Journal of Materials Chemistry A* **1**, 12327 (2013).

8 Kay, A., Cesar, I. & Grätzel, M. New Benchmark for Water Photooxidation by Nanostructured α-Fe_2O_3 Films. *J. Am. Chem. Soc.* **128**, 15714-15721 (2006).

9 Maeda, K. & Domen, K. Photocatalytic Water Splitting: Recent Progress and Future Challenges. *J. Phys. Chem. Lett.* **1**, 2655-2661 (2010).

10 Han, H. S. & et al. Boosting the solar water oxidation performance of a $BiVO_4$ photoanode by crystallographic orientation control. *Energy Environ. Sci.* **11**, 1299-1306 (2018).

11 Maeda, K. & Domen, K. New Non-Oxide Photocatalysts Designed for Overall Water Splitting under Visible Light. *The Journal of Physical Chemistry C* **111**, 7851-7861 (2007).

12 Fountaine, K. T., Lewerenz, H. J. & Atwater, H. A. Efficiency limits for photoelectrochemical water-splitting. *Nat Commun* **7**, 13706 (2016).

13 Assavachin, S., Xiao, C., Becker, K. & Osterloh, F. E. Facets control charge separation during photoelectrochemical water oxidation with strontium titanate ($SrTiO_3$) single crystals. *Energy Environ. Sci.* **17**, 3493-3502 (2024).

14 Mu, L., Zhao, Y., Li, A., Wang, S., Wang, Z., Yang, J., Wang, Y., Liu, T., Chen, R., Zhu, J., Fan, F., Li, R. & Li, C. Enhancing charge separation on high symmetry $SrTiO_3$ exposed with anisotropic facets for photocatalytic water splitting. *Energy & Environmental Science* **9**, 2463-2469 (2016).

15 Ma, T., Jacobs, R., Booske, J. & Morgan, D. Understanding the interplay of surface structure and work function in oxides: A case study on $SrTiO_3$. *APL Materials* **8** (2020).

16 Hsieh, P. L. & et al. Facet-Dependent and Adjacent Facet-Related Electrical Conductivity Properties of $SrTiO_3$ Crystals. *J. Phys. Chem. C* **125**, 10051-10056 (2021).

17 Kumar, G., Chen, Z. L., Jena, S. & Huang, M. H. Facet-dependent optical and electrical properties of $SrTiO_3$ wafers. *J. Mater. Chem. C* **11**, 3885-3888 (2023).

18 Vanacore, G. M., Zagonel, L. F. & Barrett, N. Surface enhanced covalency and Madelung potentials in Nb doped $SrTiO_3$ (100), (110) and (111) single crystals. *Surface Science* **604**, 1674-1683 (2010).

19 Roe, E. T., Egelhofer, K. E. & Lonergan, M. C. Limits of Contact Selectivity/Recombination on the Open-Circuit Voltage of a Photovoltaic. *ACS Applied Energy Materials* **1**, 1037-1046 (2018).

20 Würfel, P. & Würfel, U. *Physics of solar cells: from basic principles to advanced concepts*. 3rd edition edn, (Wiley-VCH, 2016).
21 Sze, S. M. & Ng, K. K. *Physics of Semiconductor Devices: Sze/Physics*. (John Wiley & Sons, Inc., 2006).
22 Kaufman, A. J., Krivina, R. A., Shen, M. & Boettcher, S. W. Controlling Catalyst–Semiconductor Contacts: Interfacial Charge Separation in p-InP Photocathodes. *ACS Energy Lett.* **7**, 541–549 (2022).
23 Laskowski, F. A. L., Nellist, M. R., Qiu, J. & Boettcher, S. W. Metal oxide/(oxy)hydroxide overlayers as hole collectors and oxygen-evolution catalysts on water-splitting photoanodes. *J. Am. Chem. Soc.* **141**, 1394-1405 (2019).
24 Laskowski, F. A. L., Oener, S. Z., Nellist, M. R., Gordon, A. M., Bain, D. C., Fehrs, J. L. & Boettcher, S. W. Nanoscale Semiconductor/Catalyst Interfaces in Photoelectrochemistry. *Nature Materials* **19**, 69-76 (2020).
25 Nellist, M. R., Laskowski, F. A. L., Lin, F., Mills, T. J. & Boettcher, S. W. Semiconductor–Electrocatalyst Interfaces: Theory, Experiment, and Applications in Photoelectrochemical Water Splitting. *Acc. Chem. Res.* **49**, 733-740 (2016).
26 Lin, F. & Boettcher, S. W. Adaptive semiconductor/electrocatalyst junctions in water-splitting photoanodes. *Nat. Mater.* **13**, 81-86 (2014).
27 Lin, F. & Boettcher, S. W. in *Photoelectrochemical Solar Fuel Production* (eds Sixto Giménez & Juan Bisquert) 323-351 (Springer International Publishing, 2016).
28 Axnanda, S., Crumlin, E. J., Mao, B., Rani, S., Chang, R., Karlsson, P. G., Edwards, M. O. M., Lundqvist, M., Moberg, R., Ross, P., Hussain, Z. & Liu, Z. Using "Tender" X-Ray Ambient Pressure X-Ray Photoelectron Spectroscopy as A Direct Probe of Solid-Liquid Interface. *Sci. Rep.* **5**, 9788 (2015).
29 Lichterman, M. F., Hu, S., Richter, M. H., Crumlin, E. J., Axnanda, S., Favaro, M., Drisdell, W., Hussain, Z., Mayer, T., Brunschwig, B. S., Lewis, N. S., Liu, Z. & Lewerenz, H. J. Direct Observation of the Energetics at a Semiconductor/Liquid Junction by Operando X-Ray Photoelectron Spectroscopy. *Energy Environ. Sci.* **8**, 2409-2416 (2015).
30 Hofstein, S. R. & Warfield, G. Physical limitations on the frequency response of a semiconductor surface inversion layer. *Solid-State Electron.* **8**, 321-341 (1965).
31 Mu, L., Zeng, B., Tao, X., Zhao, Y. & Li, C. Unusual Charge Distribution on the Facet of a $SrTiO_3$ Nanocube under Light Irradiation. *J Phys Chem Lett* **10**, 1212-1216 (2019).
32 Mills, T. J., Laskowski, F. A. L., Dette, C., Nellist, M. R., Lin, F. & Boettcher, S. W. The role of surface states in electrocatalyst-modified semiconductor photoelectrodes: Theory and simulations. *arXiv:1707.03112* (2017).
33 Burke, M. S., Kast, M. G., Trotochaud, L., Smith, A. M. & Boettcher, S. W. Cobalt-iron (oxy)hydroxide oxygen evolution electrocatalysts: the role of structure and composition on activity, stability, and mechanism. *J Am Chem Soc* **137**, 3638-3648 (2015).
34 Favaro, M., Yang, J., Nappini, S., Magnano, E., Toma, F. M., Crumlin, E. J., Yano, J. & Sharp, I. D. Understanding the Oxygen Evolution Reaction Mechanism on CoO_x using Operando Ambient-Pressure X-ray Photoelectron Spectroscopy. *J Am Chem Soc* **139**, 8960-8970 (2017).
35 Vadhva, P., Hu, J., Johnson, M. J., Stocker, R., Braglia, M., Brett, D. J. L. & Rettie, A. J. E. Electrochemical Impedance Spectroscopy for All-Solid-State Batteries: Theory, Methods and Future Outlook. *ChemElectroChem* **8**, 1930-1947 (2021).
36 Stoerzinger, K. A., Favaro, M., Ross, P. N., Yano, J., Liu, Z., Hussain, Z. & Crumlin, E. J. Probing the Surface of Platinum during the Hydrogen Evolution Reaction in Alkaline Electrolyte. *J Phys Chem B* **122**, 864-870 (2018).

37 Chehab, S., Canaday, J., Kuriakose, A., Ahmad, A., Wheat, T. & Komorowski, P. Impedance measurements of platinum electrodes on a solid protonic conductor. *Solid State Ionics* **59**, 125-132 (1993).
38 Lundström, I. Hydrogen Sensitive MOS-Structures. *Sensors and Actuators* **1**, 403-426 (1981).
39 Gu, H., Wang, Z. & Hu, Y. Hydrogen Gas Sensors Based on Semiconductor Oxide Nanostructures. *Sensors* **12**, 5517-5550 (2012).
40 Saeed, S. W. & Bjørheim, T. S. The Role of Space Charge at Metal/Oxide Interfaces in Proton Ceramic Electrochemical Cells. *J. Phys. Chem. C* **124**, 20827-20833 (2020).
41 Suzuki, T. T., Ohgaki, T., Adachi, Y. & Sakaguchi, I. Polarity reversal of resistance response to trace H2 gas in the air between asymmetrically shaped electrodes on rutile-TiO2 single crystal. *Journal of Applied Physics* **131**, 034501 (2022).
42 Wagner, F. T. & Somorjai, G. A. Photocatalytic and photoelectrochemical hydrogen production on strontium titanate single crystals. *J. Am. Chem. Soc.* **102**, 5494-5502 (1980).
43 Lichterman, M. F., Richter, M. H., Hu, S., Crumlin, E. J., Axnanda, S., Favaro, M., Drisdell, W., Hussain, Z., Brunschwig, B. S., Lewis, N. S., Liu, Z. & Lewerenz, H. J. An Electrochemical, Microtopographical and Ambient Pressure X-Ray Photoelectron Spectroscopic Investigation of Si/TiO_2/Ni/Electrolyte Interfaces. *J. Electrochem. Soc.* **163**, H139 (2015).
44 Wesley, T. S., Hulsey, M. J., Westendorff, K. S., Lewis, N. B., Crumlin, E. J., Roman-Leshkov, Y. & Surendranath, Y. Metal nanoparticles supported on a nonconductive oxide undergo pH-dependent spontaneous polarization. *Chem Sci* **14**, 7154-7160 (2023).
45 Wagner, F. T., Ferrer, S. & Somorjai, G. A. Photocatalytic hydrogen production from water over SrTiO3 crystal surfaces, electron spectroscopy studies of adsorbed H_2, O_2 and H_2O. *Surface Science* **101**, 462-474 (1980).
46 Favaro, M., Valero-Vidal, C., Eichhorn, J., Toma, F. M., Ross, P. N., Yano, J., Liu, Z. & Crumlin, E. J. Elucidating the alkaline oxygen evolution reaction mechanism on platinum. *J. Mater. Chem. A* **5**, 11634-11643 (2017).
47 Han, Y., Axnanda, S., Crumlin, E. J., Chang, R., Mao, B., Hussain, Z., Ross, P. N., Li, Y. & Liu, Z. Observing the Electrochemical Oxidation of Co Metal at the Solid/Liquid Interface Using Ambient Pressure X-ray Photoelectron Spectroscopy. *J Phys Chem B* **122**, 666-671 (2018).
48 Marshall, M. S. J., Becerra-Toledo, A. E., Marks, L. D. & Castell, M. R. Defects on Strontium Titanate. **58**, 327-349 (2015).
49 Lehner, J. M., Ramírez, L. P., Kubsky, S., Gallet, J.-J., Bournel, F. & Dudy, L. Environmentally Stable p(6 × 2) $SrTiO_3$(001) Surface Reconstruction with Low-Valent Ti for Photocatalytic Water Splitting. *The Journal of Physical Chemistry C* **127**, 17285-17289 (2023).
50 Shimizu, R., Iwaya, K., Ohsawa, T., Shiraki, S., Hasegawa, T., Hashizume, T. & Hitosugi, T. Effect of oxygen deficiency on $SrTiO_3$(001) surface reconstructions. *Applied Physics Letters* **100**, 263106 (2012).
51 Wang, Z., Li, F., Meng, S., Zhang, J., Plummer, E. W., Diebold, U. & Guo, J. Strain-induced defect superstructure on the $SrTiO_3$(110) surface. *Phys Rev Lett* **111**, 056101 (2013).
52 Pan, Z., A. Röhr, J., Ye, Z., S. Fishman, Z., Zhu, Q., Shen, X. & Hu, S. Elucidating charge separation in particulate photocatalysts using nearly intrinsic semiconductors with small asymmetric band bending. *Sustain. Energy Fuels* **3**, 850-864 (2019).
53 Pan, Z. & et al. Mutually-dependent kinetics and energetics of photocatalyst/co-catalyst/two-redox liquid junctions. *Energy Environ. Sci.* **13**, 162-173 (2020).